

Tube-wave Effects in Cross-Well Seismic Data

Valeri Korneev, Lawrence Berkeley National Laboratory, Berkeley, California.

ABSTRACT

The analysis of crosswell seismic data for a gas reservoir in Texas revealed two newly detected seismic wave effects, recorded 2000 feet above the reservoir. The first is that the dominant late phases on the records are the tube-waves generated in the source well and later converted into laterally propagating waves through the reservoir in gas/water saturated layers, which convert back to tube-waves in the receiver well. The tube-wave train showed good correlation with multilayered reservoir zone structure, suggesting that the recorded wave field has strong dependence on the reservoir parameters. The second effect is that the recorded field is composed of multiple low-velocity tube-waves. The modeling results suggest that imperfect cementation is the likely cause of this phenomenon.

INTRODUCTION

Tube-waves are traditionally regarded as a source of high amplitude noise in borehole seismic data and much effort typically goes into their suppression and elimination from recordings (Daley et al., 2003). Tube-waves have very large amplitudes and can propagate long distances without substantial decay. A tube-wave is an interface wave for a cylindrical interface between two media, typically a borehole fluid and surrounding elastic rock. Borehole waves were described by Lamb (1898) and were observed in the early twentieth century (Sharpe, 1942; Ording, 1953), as summarized by White (1965). Using trapped (or guided) mode analysis, the classic tube-wave can be seen as the lowest order trapped mode (Schoenberg, 1981). Higher order modes may be generated depending on material properties and source frequency. The fundamental mode is usually called a Stoneley wave (ref). Some work has been done to analyze tube-wave attributes in order to evaluate rock properties (for example, Cheng et al., 1987, Kostek et al., 1998). The

conversion of tube-waves into a coal seam trapped modes was reported by Albright and Johnson (1990).

STRATTON FIELD EXPERIMENT

The Stratton field experiment was designed in order to experimentally demonstrate the transmission and detection of guided waves in low-velocity sedimentary layers. The details of data acquisition, processing and low-velocity bed continuity study results can be found in Parra et. al. (year), Gorogy et.al (year) . The objective of this project was to establish the feasibility and benefit of using interwell guided seismic waves in characterization of Gulf Coast gas reservoirs. Target zones were selected based on geological markers, seismic reflectors and well logs from the upper Frio Formation at the Stratton gas field. It was selected because it is one of the most extensively studied and well-documented producing oil and gas fields on the Gulf Coast (Levey et al., 1994). The Stratton field consists mainly of sandstones and shales of the Frio Formation with velocity contrasts on the order of 10% to 20%. Three low-velocity intervals were identified, from top to bottom, as the V2, V5, and V12 shale zones, and were recognizable in all the wells. The three wells in Figure 1 are the wells used to conduct the interwell logging experiments and are located in almost the same vertical plane. The data were collected in the receiver wells Ward159 and Ward145, while sources were placed in the well Ward145 between the receiver wells at three positions, corresponding to the centers of target layers V2 at 3816 ft (A), V5 at 4133 ft (B) and V12 at 4570 ft (C). The source was Texaco's multiple air gun, a tool comprised of three air guns spaced 27 inches apart, which fire simultaneously with each shot.

The guided-wave signatures were related to targets arriving in the 0.6 – 0.8 s time interval. The observed seismic data indicate the presence of trapped energy in low velocity shale markers between wells 145 and 151. Guided waves in the form of leaky modes are excited, transmitted, and detected in the low-velocity shale markers at a well separation of 1730 ft (527 m). Dispersion

analysis, modeling, frequency–amplitude depth curves, well logs, and lithological information all support the results. Due to an unusually large interwell distance in the crosswell system the overall data quality was poor. Just two shots were used for stacking the data because the release of air bubbles into the borehole fluid rapidly reduced the coupling between airgun source and the formation, producing about 40% of elastic wave energy compare to a previous shot. The strongest phases in the records, which were arriving later then 0.8 s were not interpreted at the time as being out of scope of the experiment goals.

Data sets

The three data sets A145, B145 and C145 consist of 46 records each from the receivers positioned across the target layers. The upper 7 receivers had a 10 ft spacing interval, while the next 33 receivers had 2 ft spacing and the lower 6 receivers again had 10 ft spacing interval. The whole length of the receiver line for the well Ward145 was 170 ft and had the best data quality compared to the data sets A159, B159 and C159 obtained in the well Ward159, where 3-component geophones were used. The recorded signal frequency was up to 300Hz in the well Ward145 and up to 100Hz in the far well Ward159. The Ward159 data sets had 22 receiver positions with 5 ft spacing covering 115 ft of depth around each target layer.

While geophones were used in the cemented well Ward159, the attempt to cement the space around the casing in the well Ward145 failed and there was no good bonding between the casing and the formations above 5100 ft in that well. The hydrophone recording in that well had a better signal-to-noise ratio compared to the other well, which is most likely the result of the smaller source-receiver distance. On Figure 2 the low frequency (50-100Hz) filtered traces are shown for data sets A145, B145 and C145. The same data sets for the high frequency (100-160Hz) band are shown on Figure 3. There is a presence of late high amplitude arrivals in the data, which is most pronounced at low frequencies. These arrivals are concentrated in separate wavetrains,

which are denoted as W_k , where the integer index $k = 1, 2, \dots, 6$ corresponds to the order of arrival.

Data processing

The interpretation of the strong late phases arriving in the 0.8–2.0 s interval is the subject of this paper. The relatively small travel time (0.2s) for the direct P-wave arrivals suggests that the late phases belong to waves with long propagation paths and/or rather small velocities. This energy was clearly elsewhere while the direct P- waves were arriving at 0.2 s. The apparent velocities of the strongest phases around the 1 s arrival time were estimated to be in the 1300-1500 m/s range, which corresponds to propagating tube-waves. Figure 4 shows stacked amplitude spectra of traces computed with a moving 0.3 s time window for three (A145, B145, and C145) sets. The spectra show the existence of two dominant frequency ranges in the late arriving phases with central values of 60 and 110 Hz. The main feature of the panels are the high amplitude wave trains in the 40-100 Hz interval. The late wave trains with highly similar waveforms are clearly seen from this data. The traces were cross-correlated with the corresponding first arriving wavetrain interval, which allowed the measurement of the main peak traveltimes with better than 0.01 s accuracy. This interval was 0.7 – 1.3 s for A145, 0.7 – 1.3 s for A145, and 0.7 – 1.3 s for A145 datasets. The high (90-100-200-220 Hz) and low (30-40-80-90 Hz) band-pass filtered data reveal practically the same results (Figure 5), which suggests negligibly low dispersion in the frequency band under consideration. The measured travel times for the strongest central peaks are given in Table 1 and represent upward propagating waves of varying velocities.

Receiving wells ->	Ward 159	Ward 151					
Recorded waves	Wave 1	Wave 1	Wave 2	Wave 3	Wave 4	Wave 5	Wave 6
Layer V2 at 3816 ft	1.17	1.055	1.605	-	-	-	-
Layer V5 at 4133 ft	1.04	0.92	1.32	1.75	-	-	-
Layer V12 at 4570 ft	0.86	0.73	0.965	1.19	1.115	1.64	1.875

Table 1. Picked travel times [s] for the maximum energy phases.

The high degree of correlation between different wave trains W_k allows us to assume a constant frequency-independent propagation velocity along the well. Evaluation of these velocities is done in several steps. First, the travel times obtained from well Ward159 are used to determine the tube-wave velocity v_c in the cemented wells, yielding $v_c = 1460$ m/s. Then, the velocities v_k of the first three $k = 1, 2, 3$ wave-trains recorded in at least two of the target layers are determined from the equation

$$\Delta t_{ij}^{(k)} \equiv t_i^{(k)} - t_j^{(k)} = (h_i - h_j)(1/v_k + 1/v_c), \quad (1)$$

where $t_l^{(k)}$ are the recorded travel times for a wave k at a target layer l , and h_l is the depth of that layer. This allows us to evaluate the velocities for the three fastest waves and obtain the values $v_1 = 1365$ m/s, $v_2 = 470$ m/s, and $v_3 = 288$ m/s. In order to determine the depth of origin of slow wave generation, it is assumed that waves recorded in Ward145 originated at the same depth h_o , and for any target layer $i = 1, 2, 3$ we can use the equation

$$\Delta t_i^{(eq)} \equiv t_i^{(e)} - t_i^{(q)} = (h_o - h_i)(1/v_e - 1/v_q), \quad (2)$$

where indexes e and q indicate one of three recorded waves. All five possible combinations of waves (since the layer A has just two recorded waves) give very close values averaging at $h_o = 5110$ ft and varying within a 12 ft range. This value almost coincides with the 5115 ft depth of the well packer. In all of the following evaluations, the packer location is the origin of all tube-wave trains recorded in Ward145. According to well records at depths below the packer Ward145 has cementation, and therefore it is assumed that the tube-wave velocity at those depths is the same as for Ward154 and Ward159 and is equal to $v_c = 1460$ m/s. Using this assumption,

the velocities v_c of the other three wave trains ($k = 4, 5, 6$) can be estimated using the same equation (2). The results for all tube-wave velocity evaluations are shown in Table 2.

Table 2. Tube-wave velocities [m/s].

Cemented wells	Non cemented part above casing in Ward 151					
Wave 1	Wave 1	Wave 2	Wave 3	Wave 4	Wave 5	Wave 6
1460	1365	470	288	207	162	132

The almost perfect lateral homogeneity of the formation permits the interpretation of the wave propagation of late arrivals as consisting of three-leg paths. The wave propagates downward as a regular tube-wave, then converts into a horizontally propagating wave along some seismically conductive layer and after reaching the receiver well it propagates upwards, splitting into a set of at least six waves of different velocities at packer depth. The depth h_g and velocity v_g of this horizontal layer may be estimated by solving two equations of the form

$$t_i^{(w)} = (2h_g - h_o - h_i)v_c + d_w / v_g + (h_o - h_i) / v_1, \quad (3)$$

where $t_i^{(w)}$ is the travel time of a first arriving tube-wave at both receiver wells ($w = 159, 145$), and d_w is the distance between source and receiver wells ($d_{159} = 2740$ ft., $d_{145} = 1730$ ft.). The fine layered structure of the formation makes it anisotropic for wave propagation. The horizontal propagation velocity in layer g can be expressed in the form $v_g = v_v \cdot a$, where v_v is the mean velocity taken from log data and a is some unknown constant. Three independent estimates for each target layer $i = A, B, C$ gave the values $h_g = 5717$ ft. and $a = 0.63$. After obtaining these estimates, equation (3) can be used to map the recorded seismic phases from the time to the depth scale. Figure 6 shows a comparison of guided wave energy of the first train with porosity and saturation taken from well logs.

TUBE-WAVE MODELING

A solution for axial wave propagation in a layered cylinder is explored in order to explain the observed phenomena of tube-wave splitting. The solution is exact and expressed in form of an independent mode series with integer index m . It can be used for any layered models with cylindrical symmetry when the material parameters for each layer are homogeneous. The boundary conditions can be either welded or sliding, where just the normal stresses and displacements are continuous. The details of the solution are given in Appendix A. For any given frequency ω and mode index m the tube-wave velocities $v_{tw}^{(m)}$ were found as the real roots of $\Delta_m(v_{tw}^{(m)}, \omega) = 0$, where $\Delta_m(v_{tw}^{(m)}, \omega)$ is the determinant of a corresponding boundary condition problem. The root search interval is bounded below 1500 m/s, the propagation velocity of compressional waves in water.

The primary purpose of the modeling is the explanation of the six different tube-wave propagation velocities found in the Stratton experiment data. The diameter of the drill bit for this well was 25 cm and the diameter of the steel casing was 5 mm. These values, as well as the known material parameters for water, steel casing and the outer rock formation were kept unchanged. The quality of bonding between the casing and the outer rock in receiver well Ward145 is under investigation because this well is not cemented above the packer at 5100 ft. The well was drilled before 1980 and it is most likely that the space between the casing and the formation was filled by fragments of shale and sandstone as a result of sedimentation and accumulation of broken and washed out rock material. This material will be henceforth referred to as *gauge*, implying that it represents a poorly consolidated, liquid saturated mixture of sand and shale that contains gas, as the formation has some gas bearing layers. Such formations are known to have very slow P- and S- wave propagation velocities of (Berryman *year*). Several models were used in an attempt to match the observed tube-wave data, including different types of space fillings around the casing: all possible combinations of low velocity gauge, which had

either welded or sliding contacts with adjacent layers, and could also have thin liquid intermediate *skin* layers that separate gauge from casing or rock. The material parameters and sizes of the models are given in Table 3. Roots were found for the first two harmonics $m = 0, 1$. The results of computations suggest that the velocities of wave trains W_2 and W_3 are practically equal to the compressional and shear velocities of the gauge. This conclusion is supported by a typical value of v_s / v_p ratio equal to 0.62 for these two waves, and also by a perfect fit for the fastest velocity of W_1 . The thicknesses of the liquid layers had strongest impact on the velocities of W_4 , W_5 and W_6 , and were varied to find the best fit. The most interesting results for six out of the ten different models are presented in Figure 7 and the models of the bonding is shown in Table 4.

Table 3. Parameters of layers for tube-wave modeling

Material	Vp [m/s]	Vs [m/s]	Density [g/cm3]	Minimal radius [cm]	Thickness [cm]
Borehole fluid	1550	0	0.95	0	7
Steel casing	5800	3000	8	7	0.6
Fluid	1550	0	0.96	7.6	0 – 1
Gauge	540	280	1.3	7.6 – 8.6	8.4 – 6.4
Fluid	1550	0	0.96	15	0 – 1
Cement	3600	1800	2.7	7.6	8.4
Host rock	3600	1800	2.7	16	∞

Table 4. Models of material properties between casing and rock used for tube-wave modeling

Model 1	Cement
Model 2	Gauge
Model 3	Water layer - Gauge
Model 4	Gauge - Water layer
Model 5	Gauge - Water layer – Gauge

From these results it follows that only Model 4 provides a good fit for all velocities observed in the experiment. This model has sliding contact between casing and the gauge and 7 mm thick liquid skin layer separating the gauge from the host rock formation. All gauge-containing models show the fastest tube-wave velocity to be about 6% lower than in the cemented case (Model 1). Sliding-welded and welded-sliding contact models revealed just the main root for the fastest velocity. The sliding-sliding pair gave just two roots for W_5 and W_6 , but these two roots were absent for the liquid skin containing models.

DISCUSSION

The data were recorded at 2000 ft above the depleted gas reservoir. Overall the slow velocities of the tube-waves and the relatively large propagation distances explain why these waves were traveling 5 to 15 times longer than the direct P- waves. Standard cross-well surveys rely on first arriving phases for imaging and thus do not target tube-waves. The log data used for the comparison were collected 20 years before the experiment and were obtained before the reservoir exploitation. At the time of the survey most of the gas bearing layers were depleted and gas was replaced by water. Therefore, the comparison of tube-wave amplitudes and saturation data has a qualitative character indicating more the coincidence of peaks rather than their amplitude. It seems natural that the conversion of tube-waves is more effective in saturated rocks that reveal lower velocities and thus trap seismic energy. The mechanism of such conversion requires separate study.

The low values of the velocities chosen for gauge can be justified by the presence of trapped gas, as there were gas bearing layers above the packers. Even a small amount of gas present in the fluid saturated rock can dramatically decrease wave propagation velocities (Berryman *year*). It is

also likely that the gauge was unconsolidated or poorly consolidated, which also contributed in lowering of wave propagation velocities in it.

The recorded travel times of the tube-waves consistently indicate that the well packer was the source of slow tube-wave generation. The cement packer represents a strong diffractor that converts the fundamental (fastest) tube-wave into a set of slower waves, exciting an additional fundamental mode ($m=0$) related to the gauge and two modes ($m=1$) related to the liquid layer. Such waves for parallel-layer models were detected and explained by Chouet (1986) and Ferrazini and Aki (1987). They showed that waves propagating in a liquid layer between two adjacent halfspaces can have arbitrarily low velocities, which depend on the thickness of the layer. In the case of the cylindrical model, the velocity of waves in the liquid layers showed detectable sensitivity to changes as low as 1 mm in the liquid layer thickness. It seems unlikely, thought, that liquid skin layer model is an accurate representation of reality. It seems more likely that small pockets of water trapped in the gauge effectively act as a single thin layer. This is partially supported by the presence of low velocity tube-waves for the models containing a liquid layer on either side of the gauge.

CONCLUSIONS

Two main wave propagation phenomena were found in the Stratton field crosswell seismic experiment in addition to those found in a previous study of directly propagating guided waves (*ref*). The first is that the dominant late phases on the records are composed of tube-waves that are generated in the source wells and subsequently converted into waves propagating horizontally along the reservoir in gas/water saturated layers. The second phenomenon is that in a poorly bonded receiver well a phenomenon of tube-wave mode splitting was found, when six kinds of tube-waves were detected, each having a different velocity. The current study shows that the existence of these waves can be explained by the contact conditions of the borehole casing with the formation.

Because reservoir waves should be affected by reservoir properties (i.e. porosity, permeability, fracture density and orientation), monitoring based on use of these waves should allow the detection and interpretation of reservoir property changes near production boreholes. These effects can be used for the development of new and promising technology for the imaging and monitoring of underground gas, oil and water reservoirs.

ACKNOWLEDGMENTS

This work was supported by the Office of Science, Office of Basic Energy Sciences, Division of Engineering and Geosciences of the U.S. Department of Energy under Contract No.DE-AC03-76SF00098. The data were obtained with support of the Gas Research Institute, contract 5093-260-2600. Authors wish to thank Anthony Gorody for fruitful discussions and collaboration in experiment planning and data acquisition.

REFERENCES

- Albright, J. N. and P. A. Johnson, Cross-borehole observation of mode conversion from borehole Stoneley waves to channel waves at a coal layer, *Geophysical Prospecting* , **38**, 607-620, 1990.
- Buchanan, D. J., 1983, In-seam seismology: A method for detecting faults in coal seams, *in* Fitch, A. A., Ed., *Developments in geophysical exploration methods*, **5**: Applied Science Publ. Ltd., 1–34.
- Cheng, C. H. and Jinzhong, Z. and Burns, D. R., 1987, Effects of in-situ permeability on the propagation of Stoneley tube-waves in a borehole: *Geophysics*, **52**, 1279-1289.
- Coates, R. T., 1998, A modeling study of open-hole single-well seismic imaging: *Geophy. Prosp.*, **6**, 153-175.
- Chouet B., 1986. Dynamics of a fluid-driven crack in three dimensions by the finite difference method. *J. Geophys. Res.*, **91**, 13967-13992

Daley, T.M., Gritto, R. and E.L. Majer, 2003, Tube-wave suppression in single-well seismic acquisition, *Geophysics*, In print.

Dresen, L., and Ruter, H., 1994, Seismic coal exploration part B: Inseam seismic: Pergamon Press, Inc.

Ferrazini and Aki, 1987. Slow waves trapped in fluid-filled infinite-crack: implication for volcanic tremor. *J. Geophys. Res.*, **92**, B9, 9215-9223.

Gorody, A.W., and Parra, J. O., 1999, Continuity logging for mapping low velocity geological markers: *Gas Tips*, **5**, 4–10.

Goudswaard, J.C.M., ten Kroode, A.P.E., Snieder, R.K. and Verdel, A.R.: 1998, Detection of lateral velocity contrasts by crosswell travelttime tomography, *Geophysics*, **63**, 523-533.

Hardage, D. A., 1992, Crosswell seismology and reverse VSP: Geophysical Press.

Kosters, E. C., Bebout, D. G., Seni, S. J., Garrett, C. M., Jr., Brown, L. F., Hamlin, H. S., Dutton, S. P., Ruppel, S. C., Finley, R. J., and Tyler, N., 1989, Atlas of major Texas gas reservoirs: Univ. of Texas at Austin Bureau of Economic Geology.

Herman, G.C., Milligan, P.A., Dong, Q. and Rector III, J.W., 2000, Analysis and removal of multiply scattered tube-waves: *Geophysics*, **65**, 745-754.

Korneev, V.A. and Johnson L.R., 1993, Scattering of elastic waves by a spherical inclusion - 1. Theory and numerical results. *Geoph. Journ. Int.*, **115**, 230-250.

Kostek, S., Johnson, D. L. and Randall, C. J., 1998, The interaction of tube-waves with borehole fractures, Part I: Numerical models: *Geophysics*, **63**, 800-808.

Lamb, H., 1898, On the velocity of sound in a tube, as affected by the elasticity of the walls: *Manchester Memoirs*, **42**, 1-16.

Levey, R. A., Finley, R. J., and Sippel, M. A., 1994, Quantifying secondary gas resources in fluvial/deltaic reservoirs: A case history from Stratton field, south Texas: Univ. of Texas at Austin Bureau of Economic Geology, R.I. **221**.

- Mal, A. K., 1988, Guided waves in layered solids with interfacial zone: *Internat. J. Eng. Sci.*, **26**, 873–881.
- Muskat, M., 1981, *Physical principles of oil production*, International Human Resources Development Corporation., Boston.
- Parra, J. O., 1996, Guided seismic waves in layered poroviscoelastic media for continuity logging applications: *Model studies: Geophys. Prosp.*, **55**, 403–425.
- Parra, J. O., and Xu, P.-C., 1994, Dispersion and attenuation of acoustic guided waves in layered fluid-filled porous media: *J. Acoust. Soc. Am.*, **95**, 91–98.
- Parra, J. O., Sturdivant, V. R., and Xu, P.-C., 1993, Interwell seismic transmission and reflection through a dipping low-velocity layer: *J. Acoust. Soc. Am.*, **93**, 1954–1969.
- Parra, J. O., Zook, B. J., P.-C., Xu, and Brown, R. L., 1998, Transmission and detection of guided seismic waves in attenuating media: *Geophysics*, **63**, 1190–1199.
- Schoenberg, M., Marzetta, T., Aron, J., Porter, R.P., Space-time dependence of acoustic waves in a borehole: *J. Acoust. Soc. Am.*, **70**, 1496-1507.
- White, J.E., 1965, *Seismic Waves: Radiation, Transmission, and Attenuation*, McGraw-Hill, Inc., 302p. *Geophys.*, 156-159.

APPENDIX A

Cylindrical vector system

The cylindrical vector system used in this paper was introduced by Korneev and Johnson (1993). Use of these vectors makes expressions for the Lamé equation especially simple since they thoroughly imply a special symmetry of the problem. The cylindrical vector system has the form

$$\mathbf{Y}_m^0 = Y_m \mathbf{e}_3, \quad \mathbf{Y}_m^+ = Y_m \mathbf{e}_1 - Y_m \mathbf{e}_2, \quad \mathbf{Y}_m^- = Y_m \mathbf{e}_1 + Y_m \mathbf{e}_2, \quad (\text{A1})$$

where

$$Y_m \equiv Y_m(\varphi, z) \equiv \exp i(m\varphi + hz), \quad m = 0, 1, 2, \dots, \quad (\text{A2})$$

and h is the projection of the wavenumber onto the OZ-axis, $i = \sqrt{-1}$. Vectors $\mathbf{e}_1, \mathbf{e}_2, \mathbf{e}_3$ are the natural unit vectors of the cylindrical coordinate system (ρ, φ, z) .

The cylindrical vectors of the system in (A1) are orthonormal at any point on a cylindrical surface. In the space of vector functions $\vec{f}(\varphi), 0 \leq \varphi \leq 2\pi$ defined on a circle $\rho = \text{const.}, z = \text{const.}$ the vectors (A1) satisfy the following orthogonality relations

$$\int_0^{2\pi} (\mathbf{Y}_m^\nu \cdot \mathbf{Y}_{m_1}^{\nu_1}) d\varphi = c^\nu \delta_{mm_1} \delta_{\nu\nu_1}, \quad \nu = 0, +, - \quad (\text{A3})$$

where δ_{kl} is equal to 1, when lower indexes are the same, and equal zero otherwise. The normalizing coefficients c^ν are

$$c^0 = 1, \quad c^+ = 2, \quad c^- = 2 \quad (\text{A4})$$

The system (A1) is complete in the sense of convergence in the mean for a Fourier series expansion. This means that any vector function

$$\vec{u} \equiv \vec{u}(\rho, \varphi, z) = \vec{U}(\rho, \varphi) \exp i h z \quad (\text{A5})$$

can be represented in the form

$$\vec{u}(\rho, \varphi, z) = \sum_\nu \sum_{m=0}^{\infty} f_m^\nu(\rho) \mathbf{Y}_m^\nu(\varphi, z) \quad (\text{A6})$$

The Lamé equation for a homogenous elastic medium is

$$(\lambda + \mu) \nabla \nabla \cdot \vec{u} + \nabla \times \nabla \times \vec{u} + \rho \omega^2 \vec{u} = 0 \quad (\text{A7})$$

where the dependence of the displacement field \vec{u} on time t is given by $\exp(i\omega t)$, where ω is the angular frequency. The parameters λ and μ from (A7) are the Lamé constants, and ρ is the density.

Substitution of the form (A6) into equation (A7) and use of the orthogonality property (A3) yields the differential Bessel equations for radial functions $f_m^\nu \equiv f_m^\nu(\rho)$:

$$f_{mq}^0 = d_{mq}^0 Z_m(\alpha_q \rho), \quad f_{mq}^+ = d_{mq}^+ Z_{m+1}(\alpha_q \rho), \quad f_{mq}^- = d_{mq}^- Z_{m-1}(\alpha_q \rho), \quad q = p, s, \quad (\text{A8})$$

where $Z_k(x)$ - is the cylindrical Bessel functions of order k , and d_{mq}^v is an arbitrary constant, which can be determined by solving a corresponding boundary value problem. The parameter α_q from equation (A8) has two forms

$$\alpha_p = \sqrt{\omega^2 / v_p^2 - h^2}, \dots \alpha_s = \sqrt{\omega^2 / v_s^2 - h^2}, \quad (\text{A9})$$

where

$$v_p = \sqrt{(\lambda + 2\mu) / \rho}, \quad \text{and} \quad v_s = \sqrt{\mu / \rho} \quad (\text{A10})$$

are the propagation velocities of compressional (\vec{u}_p) and shear (\vec{u}_s) field components.

The simplicity of equations (A8) illustrates the main advantage of employing the cylindrical vectors of the form (A1). In all other systems the expressions for radial functions would also contain combinations of Bessel functions and their derivatives.

Fields \vec{u}_p and \vec{u}_s satisfy the equations

$$\nabla \times \vec{u}_p = 0, \quad \nabla \cdot \vec{u}_s = 0, \quad (\text{A11})$$

which leads to the following conditions

$$d_{mp}^+ \equiv a_m, \quad d_{mp}^- = -a_m, \quad d_{mp}^0 = -2ih / \alpha_p \quad (\text{A12})$$

$$d_{ms}^+ \equiv b_m, \quad d_{ms}^- \equiv c_m, \quad d_{ms}^0 = i(b_m - c_m) \alpha_s / h, \quad (\text{A13})$$

for the coefficients of equation (A8). Therefore, the fields \vec{u}_p and \vec{u}_s have the forms

$$\vec{u}_p = \sum_{m=0}^{\infty} \vec{u}_{mp} = \sum_{m=0}^{\infty} a_m \left(-\frac{2ih}{\alpha_s} Z_m(\alpha_p \rho) \mathbf{Y}_m^0 + Z_{m+1}(\alpha_p \rho) \mathbf{Y}_m^+ - Z_{m-1}(\alpha_p \rho) \mathbf{Y}_m^- \right) \quad (\text{A14})$$

$$\vec{u}_s = \sum_{m=0}^{\infty} \vec{u}_{ms} = \sum_{m=0}^{\infty} \left(\frac{i\alpha_s (b_m - c_m)}{h} Z_m(\alpha_s \rho) \mathbf{Y}_m^0 + b_m Z_{m+1}(\alpha_s \rho) \mathbf{Y}_m^+ + c_m Z_{m-1}(\alpha_s \rho) \mathbf{Y}_m^- \right) \quad (\text{A15})$$

For any index $m = 0, 1, 2, \dots$ a correspondent component \bar{u}_{mv} , $v = p, s$ of equation (A14) or (A15)

satisfies the equation of motion (A7), and represents an independently propagating harmonic of this index.

The expressions for the traction field on a surface $\rho = \text{const.}$

$$\mathbf{t}_\rho(\bar{\mathbf{u}}) = \lambda \nabla \cdot \bar{\mathbf{u}} \mathbf{e}_1 + \mu \left(2 \frac{\partial \bar{\mathbf{u}}}{\partial \rho} + \mathbf{e}_1 \times \nabla \times \bar{\mathbf{u}} \right) \quad (\text{A16})$$

expressed through vectors (A1) have the form:

$$\begin{aligned} \mathbf{t}_\rho(\bar{\mathbf{u}}_{mp}) = a_m & \left(-4i\mu h Z'_m \mathbf{Y}_m^0 + \alpha_p (\lambda(1 + h^2 / \alpha_p^2) Z_m + 2\mu Z'_{m+1}) \mathbf{Y}_m^+ \right. \\ & \left. + \alpha_p (\lambda(1 + h^2 / \alpha_p^2) Z_m - 2\mu Z'_{m-1}) \mathbf{Y}_m^- \right) \end{aligned} \quad (\text{A17})$$

$$\begin{aligned} \mathbf{t}_\rho(\bar{\mathbf{u}}_{ms}) = ih\mu & \left(b_m (Z_{m+1} + Z'_m \alpha_s^2 / h^2) + c_m (Z_{m-1} - Z'_m \alpha_s^2 / h^2) \right) \mathbf{Y}_m^0 \\ & + i\alpha_s \mu (b_m (2Z'_{m+1} - Z_m / 2) + c_m Z_m / 2) \mathbf{Y}_m^+ + i\alpha_s \mu (b_m Z_m / 2 + c_m (2Z'_{m-1} + Z_m / 2)) \mathbf{Y}_m^- \end{aligned} \quad (\text{A18})$$

In a cylindrical coordinate system, \mathbf{t} is given by:

$$\begin{aligned} \mathbf{t}_\rho(\bar{\mathbf{u}}_{mp}) = a_m & \left(2\alpha_p (\lambda(1 + h^2 / \alpha_p^2) Z_m + \mu(Z'_{m+1} - Z'_{m-1})) Y_m \mathbf{e}_1 \right. \\ & \left. - 2i\alpha_p \mu (Z'_{m+1} + Z'_{m-1}) Y_m \mathbf{e}_2 - 4i\mu h Z'_m Y_m \mathbf{e}_3 \right) \end{aligned} \quad (\text{A19})$$

$$\begin{aligned} \mathbf{t}_\rho(\bar{\mathbf{u}}_{ms}) = 2\alpha_s \mu & (b_m Z'_{m+1} + c_m Z'_{m-1}) Y_m \mathbf{e}_1 + i\alpha_s \mu (b_m (Z_m - 2Z'_{m+1}) + c_m (Z_m + 2Z'_{m-1})) Y_m \mathbf{e}_2 \\ & + ih\mu (b_m (Z_{m+1} + Z'_m \alpha_s^2 / h^2) + c_m (Z_{m-1} - Z'_m \alpha_s^2 / h^2)) Y_m \mathbf{e}_3 \end{aligned} \quad (\text{A20})$$

in unit vectors of cylindrical coordinate system. Arguments of the Bessel functions and their derivatives are equal to $\alpha_p \rho$ for equations (A17) and (A19) and are equal to $\alpha_s \rho$ for equation (A18) and (A20).

Boundary value problem

Consider a model consisting of N cylindrical layers characterized by constant parameters $\lambda_n, \mu_n, \rho_n, n=1, \dots, N$ and separated by interfaces $r = r_n, n = 1, \dots, N-1$. In each layer the elastic wave field can be expressed through equations (A17), (A18), where the radial functions depend on the parameters of each particular layer. In the fluid-bearing layers we have $\mu_n = 0$ and $b_m = c_m = 0$. For $n=1$, the function $Z_k(x)$ must be finite for $r=0$ and $Z_k(x) = J_k(x)$. For the outermost medium, the wave field must satisfy the radiation condition at infinity $r = \infty$, and $Z_k(x) = H_k^{(2)}(x)$. In the cases where the intermediate layers are bounded by two interfaces, any two independent solutions for the radial functions $Z_k(x)$ must be used, thereby doubling the number of coefficients a_m, b_m, c_m for that layer. According to equation (A8) the arguments of the Bessel functions can be either real or imaginary, depending on the value of the vertical wave number h .

For fluid-solid interfaces the boundary conditions have the form

$$\sum_{i=n}^{n+1} (\vec{u}^{(i)})_r = 0, \quad \sum_{i=n}^{n+1} (\mathbf{t}^{(i)})_r = 0, \quad (\mathbf{t}^{(n+1)})_\varphi = 0, \quad (\mathbf{t}^{(n+1)})_z = 0, \quad r = r_n, \quad n = 1, \dots, N-1 \quad (\text{A21})$$

while for solid-solid welded contact they are

$$\sum_{i=n}^{n+1} \vec{u}^{(i)} = 0, \quad \sum_{i=n}^{n+1} \mathbf{t}^{(i)} = 0, \quad r = r_n, \quad n = 1, \dots, N-1 \quad (\text{A22})$$

Orthogonality of cylindrical vectors allows to reduce equations (A21) and (A22) to the separate forms

$$\sum_{i=n}^{n+1} (\vec{u}_m^{(i)})_r = 0, \quad \sum_{i=n}^{n+1} (\mathbf{t}_m^{(i)})_r = 0, \quad (\mathbf{t}_m^{(n+1)})_\varphi = 0, \quad (\mathbf{t}_m^{(n+1)})_z = 0, \quad (\text{A23})$$

$$r = r_n, \quad n = 1, \dots, N-1$$

and

$$\sum_{i=n}^{n+1} \vec{u}_m^{(i)} = 0, \quad \sum_{i=n}^{n+1} \mathbf{t}_m^{(i)} = 0, \quad r = r_n, \quad n = 1, \dots, N-1 \quad (\text{A24})$$

for each harmonic m .

For a set of coefficients $a_m^{(n)}, b_m^{(n)}, c_m^{(n)}$ the conditions (A23) and (A24) give a homogeneous system of linear equations. Taking h to be

$$h = \frac{\omega}{v_{\text{tw}}^{(m)}}, \quad (\text{A25})$$

where $v_{\text{tw}}^{(m)}$ is the vertical phase velocity of the tube waves, the velocities of the propagating tube-waves can be found to be the roots of the equation $\Delta_m(v_{\text{tw}}^{(m)}, \omega) = 0$, where $\Delta_m(v_{\text{tw}}^{(m)}, \omega)$ is the determinant of the above mentioned linear system.

Figure captions

Figure 1 Data acquisition scheme for the Stratton cross well experiment. Sources and receivers were placed at the upper low-velocity layers V2, V5 and V12. The reservoir layers are below the depth of 5100 ft where all the wells had packers.

Figure 2 Single shot gathers in 50-100 Hz frequency band for the receiver well Ward 145.

Traces recorded in V2 (a), V5 (b) and V12 (c) contain high amplitude slower arrivals (wavetrains) W1-W6.

Figure 3 Same as for Figure 2, but filtered at higher 100-160 Hz frequency band.

Figure 4 Stacked frequency spectra, as functions of time, for the traces recorded in V2, V5 and V12 layers.

Figure 5 Stacked cross-correlation of traces with W1 waveform. Low band pass filtered (50-100 Hz, solid curves) and high band pass filtered (100-160 Hz, dashed curves) data produce the same peak positions.

Figure 6 Depth migrated amplitude of W1 wavetrain compared with porosity and saturation log data for Ward 145. Peak positions correlate rather well.

Figure 7 Logarithm of determinants as function of velocity V_{tw} at a frequency of 90 Hz frequency. Notches indicate tube-wave propagation velocities. Vertical lines indicate the wave train velocities of W1-W6 measured in the field experiment. Each bonding set is represented by the fundamental $m=0$ mode (thick solid lines) and first $m=1$ mode (thin solid line). The parameters of model 4 gave the best fit.

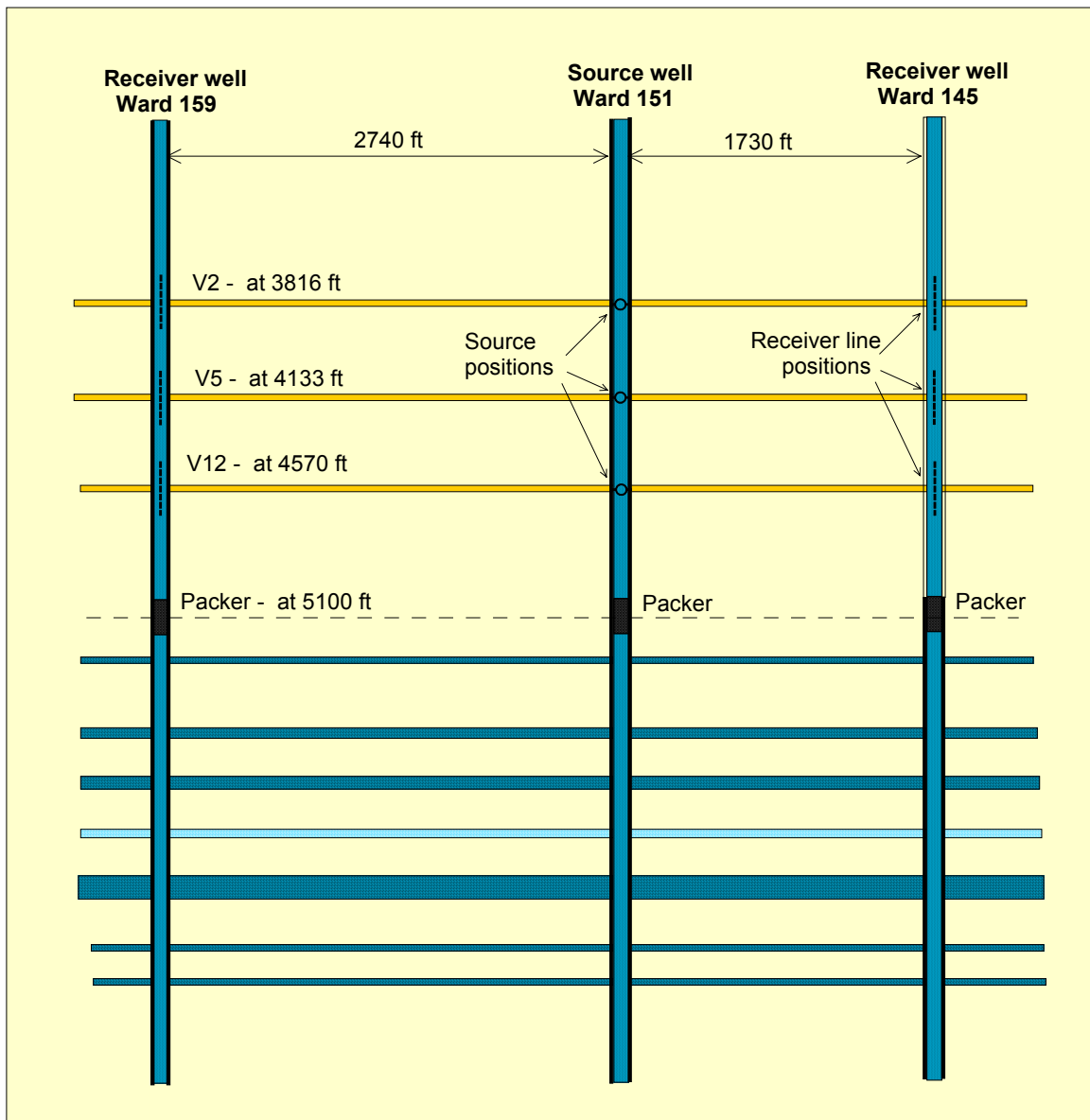


Figure 1

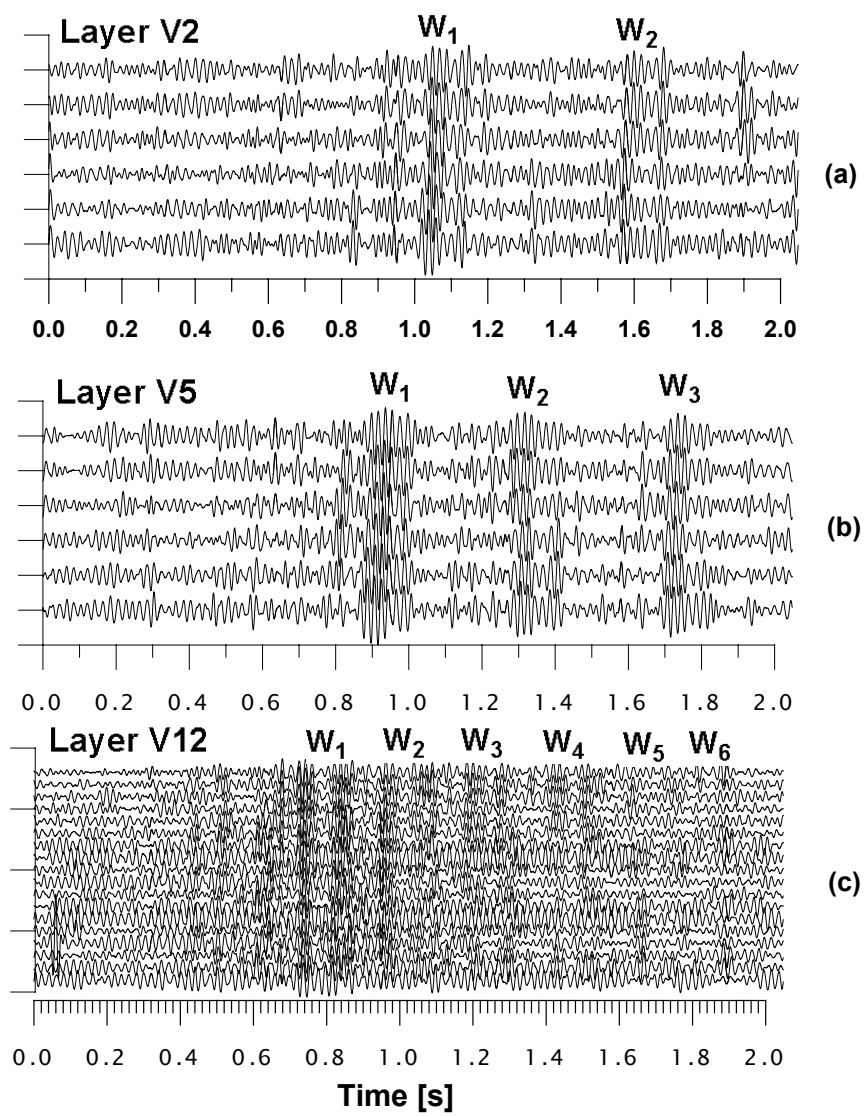


Figure 2

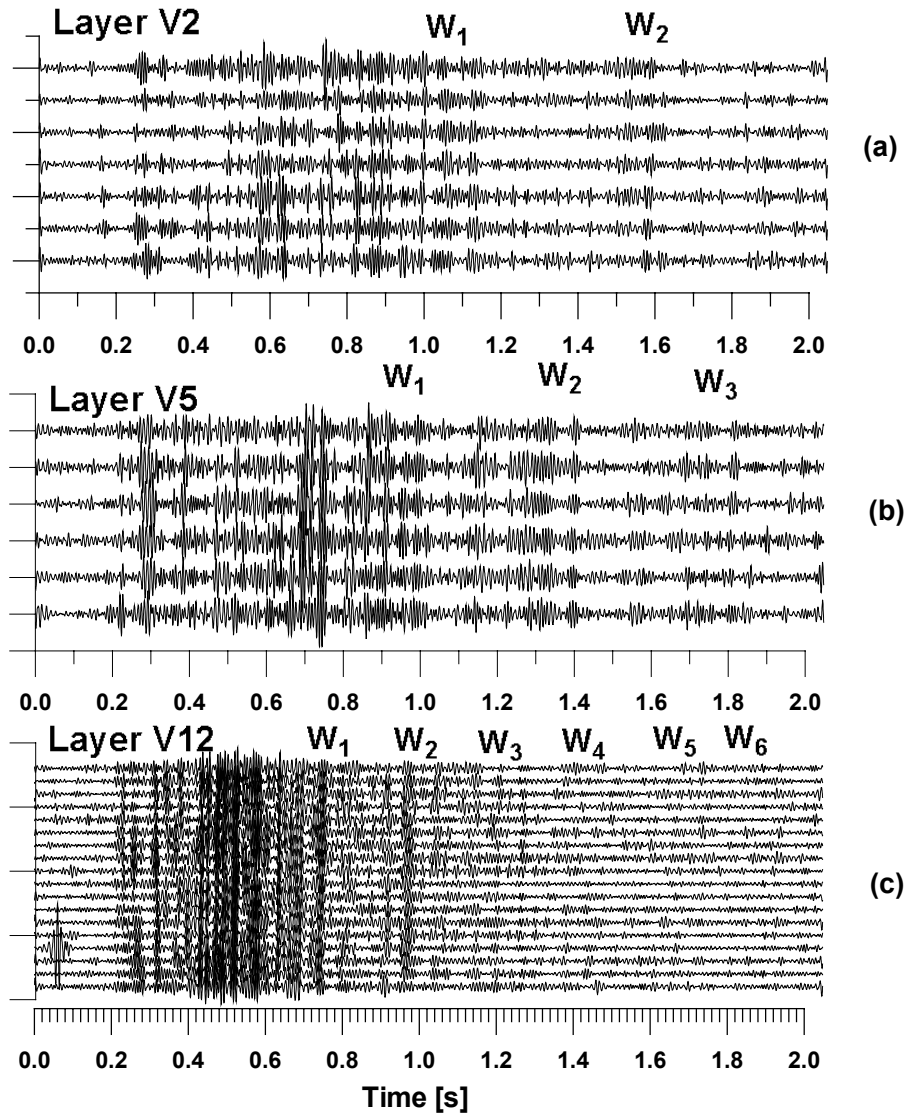


Figure 3

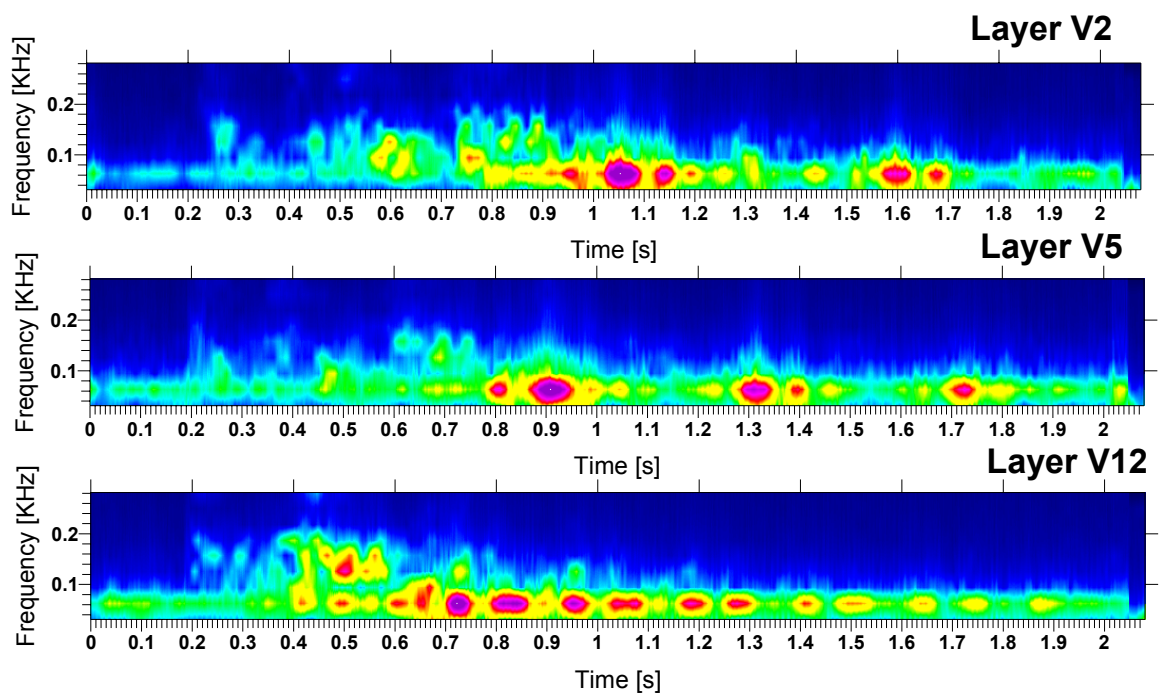


Figure 4

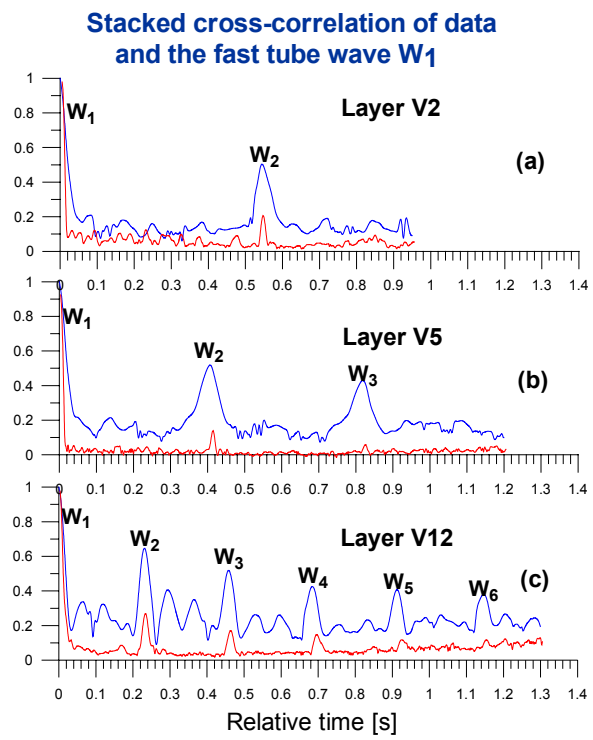


Figure 5

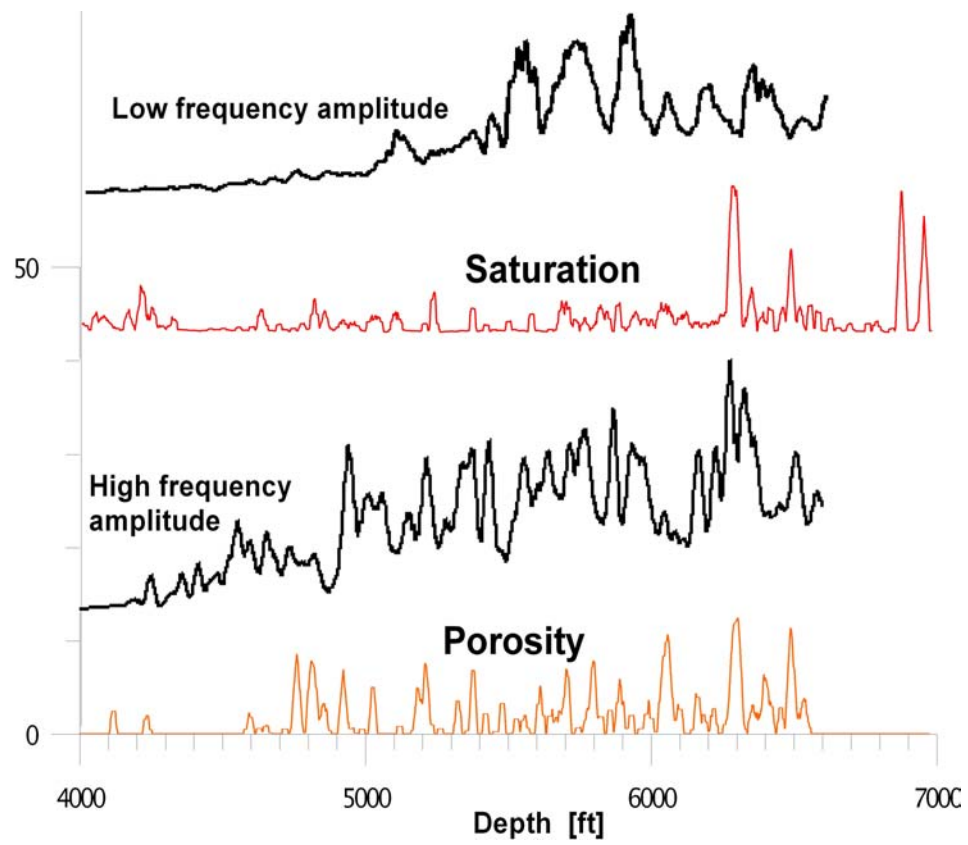


Figure 6

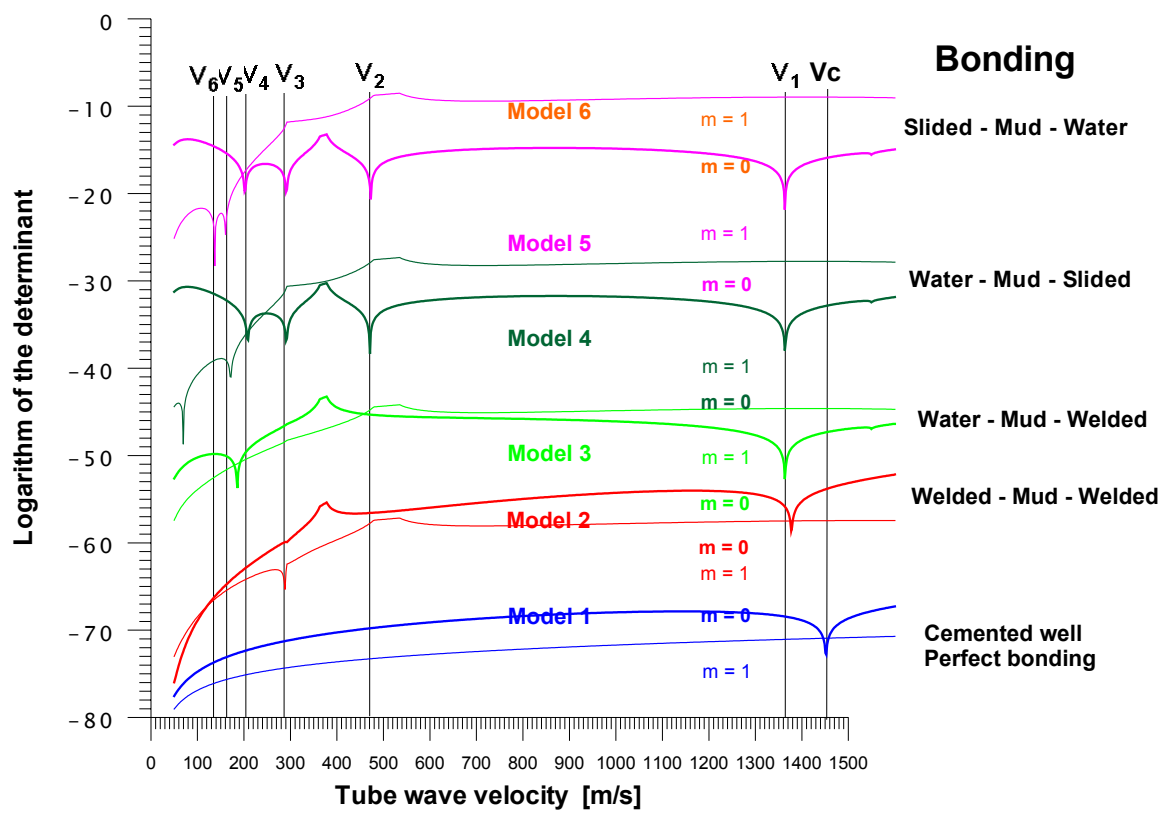


Figure 7